

Cite this: *J. Mater. Chem. A*, 2019, 7, 16472

Diversities of stoichiometry and electrical conductivity in sodium sulfides†

HPSTAR
848-2019Biao Wan,^{‡ab} Shishuai Xu,^{‡ab} Xiaohong Yuan,^{‡b} Hu Tang,^b Dajian Huang,^b Wenju Zhou,^b Lailei Wu,^{*a} Jingwu Zhang^{*a} and Huiyang Gou^{*b}

Aiming at developing and understanding the active materials in the renewable energy-storage sodium–sulfur (Na–S) system, we systemically explored the phase diversity, electronic properties, and chemical bonding of the Na–S system at ambient and high pressure up to 50 GPa, using a combination of first-principles calculations with extensive structural searches. We identified four new stable phases; Na₃S, Na₅S₃, Na₂S₂ and Na₂S₃. The previously unidentified Na₂S₃ with S₃²⁻ polyanions shows *Pnma* symmetry with quite a low formation enthalpy relative to Na₂S₂ and Na₂S₄. The simulated voltage through Na₂S₄ to generate Na₂S₃ in a battery is predicted to be 1.65 V, consistent with previous measurements. The predicted tetragonal Na₅S₃ with infinite S chains has mixed valence states of sulfur atoms, which was first observed in alkali metal sulfides. Na₃S exhibits a potential one-dimensional (1-D) electride with the chemical formula of [Na₃S]⁺·e⁻, where the sulfur atoms possess the highest coordination number (Na₁₂S). Both Na₃S and Na₅S₃ exhibit intrinsic metallic behaviors, clearly differing from other semiconducting phases. A detailed analysis of the electronic structure reveals the distinct electrical pathways of a 1-D electron gas in the channel voids in Na₃S and infinite sulfur chains with metallic S–S bonding in Na₅S₃. Our results may help to discover new candidates in Na–S systems and elucidate the potential electrochemical mechanism in the Na–S battery.

Received 3rd June 2019
Accepted 16th June 2019

DOI: 10.1039/c9ta05907e

rsc.li/materials-a

Introduction

Lithium–sulfur (Li–S) and sodium–sulfur (Na–S) batteries are currently active candidates for solid-state batteries, characterized by their high ionic conductivity, long cycle-life, and high specific energy. Due to the low material cost, Na–S batteries have ignited tremendous interest in recent years.^{1–4} Na–S batteries have already been used as energy storage devices with β"-alumina as an electrolyte.⁵ However, their use is limited by several shortcomings, for example, the high operating temperature (>300 °C), leading to safety challenges during operation.⁶ Moreover, due to the formation of solid-state Na₂S₂ (high melting point) during the discharge process,⁷ the capacity in practice is limited to 558 mA h (g of S)⁻¹, much lower than the theoretical capacity (1672 mA h g⁻¹). Great efforts have been made to develop room-temperature Na–S batteries and promote the low utilization rate of sulfur active materials,^{8–10} making the Na–S battery a promising candidate for solid-state batteries. In

Na–S batteries, multiple Na–S compounds are found in the charge/discharge process, such as Na₂S, Na₂S₂, Na₂S₄, and Na₂S₅.^{1,11,12} For Na₂S₃, previous X-ray diffraction did not support its existence, and the solid-state composition products with the composition of Na₂S₃ are believed to be the eutectic mixture of Na₂S₂ and Na₂S₄.^{13–15} On the other hand, Na₂S₃ was observed during the charge/discharge process in Na–S batteries.^{1,8,9} Moreover, Na₂S₃·NH₃ containing S₃²⁻ polyanions has been prepared at 300–320 K and 2000 bar, and the ammonia can be gently removed at 370 K.¹⁶ Therefore, a complete structural interpretation of Na₂S₃ needs to be made.

High pressure can discover and synthesize new materials with excellent physical and chemical properties, which is also applied in the discovery of novel electrodes, *e.g.* Li₁₅Si₄,^{17,18} Li₂MnO₃,¹⁹ and rutile-like CoO₂ (ref. 20) Under compression, materials usually undergo an interesting variation of electronic properties, such as the pressure-induced insulator-metal transition.²¹ For example, the semiconductors of group-VI elements of O,²² S,²³ Se,^{24,25} and Te²⁶ can be converted into metallic states under pressure, and the conductive mechanism of these elements is attributed to the insulator–metal Mott transitions at high pressure.²⁷ Electron conductivity is essential for electrodes during the battery cycle. However, both the Na–S compounds and S active materials are semiconductors, lacking intrinsic electronic conductivity.¹² Thus, sulfur active materials need additional materials to provide an electronic conductive

^aKey Laboratory of Metastable Materials Science and Technology, College of Material Science and Engineering, Yanshan University, Qinhuangdao 066004, China. E-mail: will@ysu.edu.cn; zjw@ysu.edu.cn

^bCenter for High Pressure Science and Technology Advanced Research, Beijing 100094, China. E-mail: huiyang.gou@hpstar.ac.cn

† Electronic supplementary information (ESI) available: See DOI: 10.1039/c9ta05907e

‡ B. W., S. S. X., and X. H. Y. contributed equally.

pathway, such as acetylene black and graphite.^{5,8,28} Searching for metallic Li/Na–S compounds and understanding their underlying conductive mechanism are thus critical for practical applications. Li–S compounds under ambient conditions are semiconducting,²⁹ while metallic stoichiometries (*e.g.*, Li₅S, Li₃S, and LiS₃) stabilize around 50 GPa. Under further compression to megabar pressures, all the stable Li–S phases convert to metals.³⁰ When Na₂S is studied under pressure, both the high-pressure phases (*Pnma*- and *P6₃/mmc*-type Na₂S) are semiconducting;³¹ hitherto, there are no reported metallic phases yet. A comparison study of the structural differences of the Li/Na–S compounds enables us to comprehend the energy storage mechanism and design new electrode materials. Investigations of the electronic properties and chemical bonding associated with the energy storage for all Na–S compounds are also required under both ambient and high pressure.

To explore the phase space, the electronic properties, and chemical bonding of Na–S phases at ambient and high pressure, we performed a systematic structural search at ambient and high pressure up to 50 GPa, which is accessible in current high-pressure experiments. The crystal structure searches were conducted using the *ab initio* evolutionary algorithm USPEX³² and swarm intelligence based CALYPSO^{33,34} methods, which have been widely used for the discovery of new phases. Here, we identified four new phases of NaS; Na₃S (*P6₃/mmc*), Na₅S₃ (*I4/mcm*), Na₂S₂ (*Pbam*), and Na₂S₃ (*Pnma*), which stabilized at 23.8 GPa, 3.2 GPa, 7.0 GPa, and 0.9 GPa, respectively. Among them, Na₃S is a 1-D electride with the chemical formula of [Na₃S]⁺·e[−]; Na₂S₃ can be produced under non-equilibrium conditions, which possesses quite a low formation enthalpy. Furthermore, the electronic properties reveal two metallic Na–S compounds, *i.e.*, Na₃S (*P6₃/mmc*) and Na₅S₃ (*I4/mcm*). Their metallic characteristics stem from two distinct conductive mechanisms of the one-dimensional (1-D) electron gas in the interstitial voids in Na₃S, and the conductive infinite sulfur chains in Na₅S₃. Our results provide fundamental insights into the phase diversity and electronic properties of Na–S systems.

Computational method

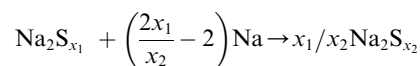
We utilized variable- and fixed-composition structure searching, using the following sequence: first, we carried out three unbiased crystal structure searches with variable compositions as implemented in the USPEX code.³² The pressure was set at 0, 20, and 50 GPa, respectively, with less than 40 atoms. Second, we performed structure searches with fixed compositions, using the CALYPSO algorithm.^{33,34} The compositions of Na : S were set as 4 : 1, 3 : 1, 2 : 1, 5 : 3, 1 : 1, 2 : 3, 1 : 2, 1 : 3, and 1 : 4, respectively. These compositions are either frequently observed in similar compounds or found to have lower formation enthalpy based on previous structure searches (variable compositions). The formation enthalpy per atoms for all Na–S phases was calculated with the equation below:

$$\Delta H(\text{Na}_x\text{S}_y) = \frac{H(\text{Na}_x\text{S}_y) - xH(\text{Na}) - yH(\text{S})}{(x + y)}$$

where H denotes the enthalpy per chemical unit for each stoichiometry, and ΔH is the formation enthalpies per atom. The sulfur phases are α -S, S-II, and S-III in pressure ranges of 0–2 GPa, 2–20 GPa, and 20–50 GPa, respectively.^{30,32} We selected sodium with a body-centered cubic (b.c.c.) structure as the reference phase.³⁵ Based on the formation enthalpies, a convex hull can be constructed. The phases staying on the convex hull are believed to be thermodynamically stable; while the phases staying above the convex hull are unstable and tend to decompose into stable compositions.

Structure relaxations and electronic structure calculations were performed using the Vienna *Ab initio* Simulation Package (VASP).^{36,37} The electron exchange–correlation interactions were treated using the generalized-gradient approximation with the Perdew–Burke–Ernzerhof functional (GGA–PBE). The vdW (optB86–vdW)^{38,39} interaction corrections were adopted to ensure the accuracy of the total energies and forces for the atoms. The PAW potentials with valence electrons of Na: 2p⁶, 3s¹ and S: 3s², 3p⁴ were used.^{40,41} A plane-wave cutoff energy of 600 eV and Monkhorst–Pack⁴² Brillouin zone sampling grid with a resolution around $2\pi \times 0.03 \text{ \AA}^{-1}$ were used to ensure that the enthalpy calculations converged well within 1 meV per atom. The dynamic stabilities of these predicted phases are evaluated by the calculations of their phonon dispersion using PHONOPY code.⁴³ The crystal-orbital Hamilton-population (COHP) analyses and integrated crystal-orbital Hamilton population (ICOHP) of Na₂S₂ (*P6₃/mmc*) and the predicted Na₅S₃ were calculated using the LOBSTER program.^{44–46} The COHP curves provide a quantitative measure of bond strengths (–COHP plotted here); the bonding states show positive –COHP while the antibonding states have negative –COHP values.

The discharging reactions between Na₂S_{x₁} and Na₂S_{x₂} ($x_1 > x_2$) in battery reactions are assumed to be:



Thus, the voltage, V , is derived using the following equation:

$$V = -\frac{x_1 E(\text{Na}_2\text{S}_{x_2}) - x_2 E(\text{Na}_2\text{S}_{x_1})}{2x_1 - 2x_2} + E(\text{Na})$$

where E denotes the total energies per chemical unit for each stoichiometry; and the pV and thermal energy contributions are neglected at zero kelvin.⁴⁷

Results and discussion

Phase stability and structure properties

The thermodynamic stabilities of the Na–S phases are verified by the calculations of formation enthalpies (ΔH). The convex hull is constructed using the generated structures in a variable-composition structure search at 0 GPa (Fig. 1a). The experimental Na₂S, Na₂S₂, Na₂S₄ and Na₂S₅ phases are thermodynamically stable. Moreover, two unidentified phases of Na₂S₃ and NaS₃ are predicted to sit above the convex hull slightly, which coincide well with the observations of these compositions during the electrochemical process.⁹ We also extend the

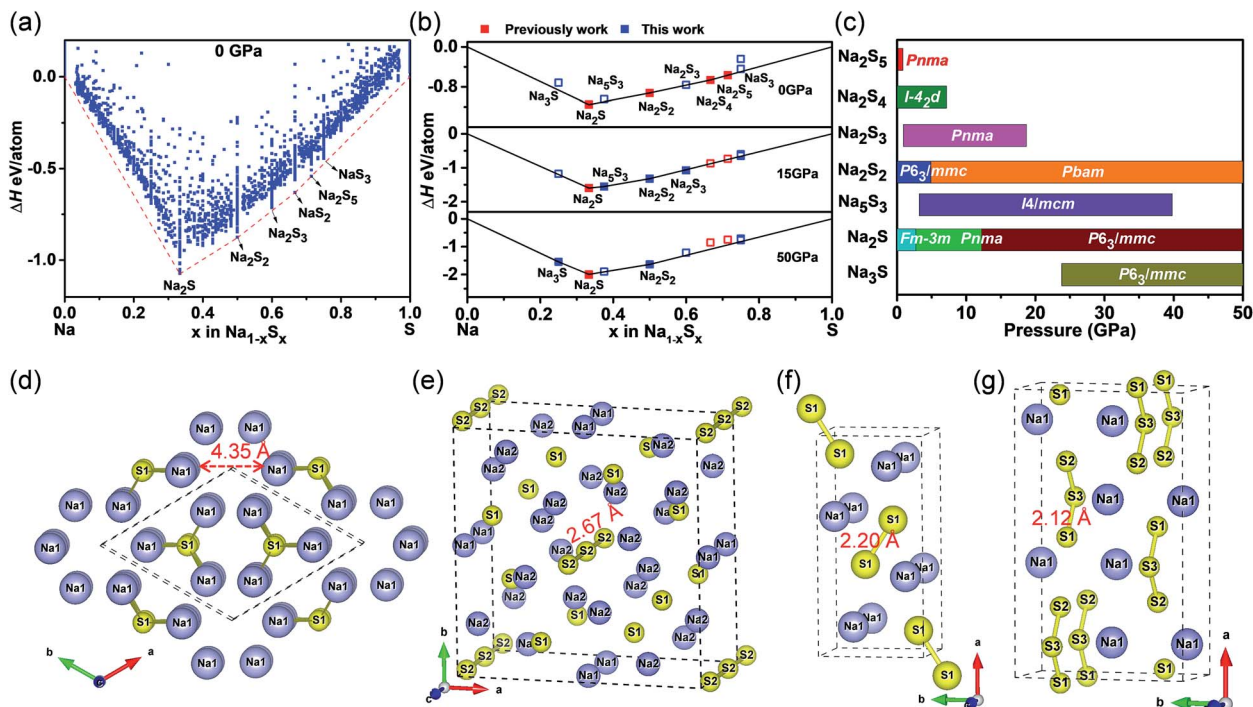


Fig. 1 (a) Convex hull constructed by structure searches using variable compositions at 0 GPa. (b) Convex hull of the Na–S system at 0 GPa, 20 GPa, and 50 GPa. Filled squares are stable phases; open squares are metastable phases at corresponding pressure. (c) Pressure–composition phase diagram of the Na–S system. Crystal structures of predicted structures (d) Na_3S , (e) Na_2S_2 , (f) Na_5S_3 and (g) Na_2S_3 .

convex hull to 50 GPa using the generated structures (Fig. S1†). Two new stoichiometries of Na_3S and Na_5S_3 stand out under pressure. Generally, sodium-rich compounds are closer to the convex hull than sulfur-rich compounds and thus under pressure, Na-rich compounds are more energetically preferable than S-rich compounds in Na–S systems. Through calculations of the formation enthalpies of Na–S phases at various pressures, we construct the convex hull (Fig. 1b) and pressure–composition phase diagram (Fig. 1c) at ambient and high pressure, using the available experimental and predicted phases. Consistent with the experimental results, all the known experimental structures Na_2S_5 , Na_2S_4 , Na_2S_2 , and Na_2S are thermodynamically stable at ambient pressure. Furthermore, we successfully reproduced the phase transformations of Na_2S at 2.7 and 12.2 GPa ($Fm\bar{3}m$ – $Pnma$ – $P6_3/mmc$), agreeing well with experimental observations (about 7.0 and 16.6 GPa).³¹ The experimental Na_2S_2 phase ($P6_3/mmc$) becomes metastable above 7.0 GPa, which transforms into a new $Pbam$ -type structure with a volume collapse of 3.6%. The experimental Na_2S_4 and Na_2S_5 phases become metastable at 7.2 GPa and 0.9 GPa, respectively. The lattice parameters of the experimental Na_2S_5 , Na_2S_4 , Na_2S_2 , and Na_2S phases calculated by the PBE and optB86-vdW method are listed in Table S1† and compared with the experimental results. Both the lattice parameters within the PBE and optB86-vdW methods are well consistent with the experimental data within a difference of 1.8% and 0.6%, respectively.

The four predicted phases of Na_3S ($P6_3/mmc$), Na_5S_3 ($I4/mcm$), Na_2S_2 ($P6_3/mmc$), and Na_2S_3 ($Pnma$) stabilized at 23.8 GPa, 3.2 GPa, 7.0 GPa, and 0.9 GPa, respectively. Interestingly, Na_2S_3

is metastable under ambient conditions and can be decomposed into Na_2S_2 and Na_2S_4 , consistent with the absence of solid-state Na_2S_3 in the experiment.^{13–15} However, Na_2S_3 possesses quite low formation enthalpy relative to Na_2S_2 and Na_2S_4 ($\text{Na}_2\text{S}_2 + \text{Na}_2\text{S}_4 \rightarrow 2\text{Na}_2\text{S}_3$; $\Delta H = 4.8$ meV per atom). The extremely low stable pressure (0.9 GPa) and formation enthalpy of Na_2S_3 explain the previous preparation of $\text{Na}_2\text{S}_3 \cdot \text{NH}_3$ ($C2/m$) at 300–320 K and a pressure of 2000 bar in liquid ammonia.¹⁶ Since the ammonia in $\text{Na}_2\text{S}_3 \cdot \text{NH}_3$ can be gently removed at 370 K, we constructed a hypothetical Na_2S_3 structure by removing the ammonia part in $\text{Na}_2\text{S}_3 \cdot \text{NH}_3$. Interestingly, after full structure relaxation, the hypothetical Na_2S_3 converts to the predicted structure. $Pnma$ -type Na_2S_3 is thus believed to exist under non-equilibrium conditions. In Na–S batteries using liquid electrolytes, polysulfides (Na_2S_n , $4 \leq n \leq 8$) with a sulfur/long chain were found during the electrochemical process.¹⁰ Like the experimental observations, two NaS_3 ($Pna2_1$ and $P4/mmm$) phases that contain S–S infinite chains ($Pna2_1$) and networks ($P4/mmm$) (Fig. S2†) are metastable with slightly higher energy above the convex hull (4.2 meV, Fig. 1b) at 0 GPa. The relatively low formation enthalpy of solid-state NaS_3 is consistent with the presence of polysulfides in the electrochemical process.

The crystal structure of the newly identified candidates for Na_3S ($P6_3/mmc$), Na_5S_3 ($I4/mcm$), Na_2S_2 ($Pbam$), and Na_2S_3 ($Pnma$) are shown in Fig. 1d–g; the detailed atomic positions of these compounds are listed in Table S2.† For Na_3S (Fig. 1d), the sulfur atoms in the host structure possess the highest coordination number (Na_{12}S) among the known Na–S phases. Moreover, atomic channel voids (diameter: 4.35 Å) constituted by

sodium atoms are observed along the *c*-axis, which definitely facilitates Na ion transport in Na–S batteries, once experimentally realized. These large interstitial voids are unique and have never been observed in Li₃S (*Pm* $\bar{3}$ *m*, *I4/mmm*, and *Fm* $\bar{3}$ *m*) and K₃S (*Pm* $\bar{3}$ *m* and *I4/mmm*) in the Li–S³⁰ and K–S⁴⁸ systems before. Following the conventional ionic charges of the Na and S atoms, Na₃S would have one excess electron per formula unit. The large interstitial voids and excess electrons make Na₃S a potential electride, which is verified by our subsequent electronic analysis. Na₅S₃ crystallizes in *I4/mcm* symmetry with infinite S–S chains (Fig. 1e) when the S concentration is further increased. A similar configuration is also found in K₅Te₃ (*I4/m*) containing infinite Te–Te chains.⁴⁹ Two kinds of non-equivalent sulfur atoms exist in Na₅S₃ and are located at Wyckoff positions of 8h (S₁) and 4a (S₂), respectively. The nearest S₂ atoms form infinite chains with a S–S separation of 2.67 Å, much longer than the semiconducting α -S phase (2.06 Å).⁵⁰ For Na₂S₂ (*Pbam*), the nearest sulfur atoms are condensed into S₂²⁻ polyanions with a S–S separation of 2.19 Å (Fig. 1f). Each sulfur atom is coordinated by eight sodium atoms (Na₈S), much higher than the ground-state phase of *P6₃/mmc*-Na₂S₂ (Na₆S). The dense crystal structure of Na₂S₂ (*Pbam*) supports its phase stability under compression. Na₂S₃ takes the same structure as K₂Te₃ (*Pnma*) (Fig. 1g). Like BaS₃ (ref. 51) and K₂S₃,⁵² the sulfur atoms in Na₂S₃ form S₃²⁻ polyanions with a S–S separation of 2.11 Å.

To verify the mechanical stability of the predicted phases of Na₃S (*P6₃/mmc*), Na₅S₃ (*I4/mcm*), Na₂S₂ (*Pbam*), and Na₂S₃ (*Pnma*), the individual elastic constants were calculated and are listed in Table S3.† All of these predicted phases follow the Born–Huang criteria,⁵³ demonstrating their mechanical stability. The bulk moduli, *B*, are 31.0 GPa, 32.1 GPa, 31.4 GPa, 28.6 GPa, 19.6 GPa, and 22.1 GPa for experimental phases Na₂S (*Fm* $\bar{3}$ *m*), Na₂S (*Pnma*), Na₂S (*P6₃/mmc*), Na₂S₂ (*P6₃/mmc*), Na₂S₄ (*I4₂d*), and Na₂S₅ (*Pnma*), respectively. The new predicted phases of Na₃S (*P6₃/mmc*), Na₅S₃ (*I4/mcm*), Na₂S₂ (*Pbam*), and Na₂S₃ (*Pnma*) have a *B* of 20.8 GPa, 36.0 GPa, 34.7 GPa, and 20.4 GPa, respectively. Among them, the greatest *B* value suggests that metallic Na₅S₃ with a small volume change against strains may be a good electrode material. Furthermore, the dynamic stability of these predicted phases is also verified by the absence of imaginary modes in the whole Brillouin zone (Fig. S3a–c†).

Electronic conductivity

Metallic Na₃S. The electronic structure of Na₃S is plotted in Fig. 2. Unlike the semiconducting Na–S phases at the ground state, Na₃S shows intrinsic metallic character, reflected by the valence bands across the Fermi level (Fig. 2a) and a finite value of the total density of states (TDOS) at the Fermi level (Fig. 2b). Due to the valence band (marked by a green curve) being degenerated with the conductive bands around the Fermi level, the Fermi surface (Fig. 2c) exhibits a planar motif. We also checked the electronic structure by SOC and HSE06 functions⁵⁴ with no band gap opening. To uncover the origin of the metallic character in Na₃S, we calculated the electron localization function (ELF)⁵⁵ and partial charge density (Fig. 2d). As shown in the ELF mappings (Fig. 2d, left), the high value of the ELF maxima

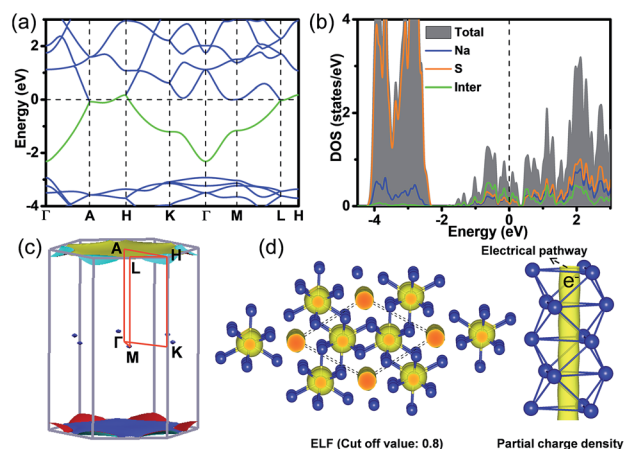


Fig. 2 Electronic properties for Na₃S. (a) Band structures. (b) Total and partial density of states (TDOS and PDOS). (c) Fermi surface. (d) ELF mappings (left) and partial charge density (right). The contribution of ‘interstitial electrons’ to the density of states is marked by ‘inter’. The green and yellow atoms represent sodium and sulfur atoms, respectively.

off the nucleus can be observed in the atomic channel voids. Moreover, the partial charge density of the valence band across the Fermi level (Fig. 2d, right) reveals that there is a one-dimensional (1-D) electron gas distribution in the channel voids, serving as an interesting electrical pathway. The partial charge density and ELF analysis suggest that Na₃S is a potential electride.^{56,57} The electrons that are confined in the channel voids are termed ‘interstitial electrons’, while the bands holding the ‘interstitial electrons’ can be regarded as ‘interstitial bands’. In electrides, the ‘interstitial electrons’ act as pseudo-atoms and occupy the crystallographic sites,⁵⁸ where the atomic channel voids are constructed by the Na octahedron serve as crystallographic cages in Na₃S (Fig. 2d). The formation mechanism of ‘interstitial electrons’ is described by Miao and Hoffmann,^{59,60} where the energy of the interstitial space and valence orbitals of the atoms will vary under pressure, and when the energy of interstitial space possesses lower energy, ‘interstitial electrons’ can form. In Na₃S, the applied pressure leads to the confinement of Na-3s electrons in the channel voids to form ‘interstitial electrons’. The connecting 1-D electron gas suggests a typical 1-D electride of Na₃S, which is also observed in Y₂Cl₃,⁵⁸ [La₈Sr₂(-SiO₄)₆]⁴⁺·e⁻,⁵⁶ Y₅Si₃ (ref. 61) and Ba₃SrN₃.⁶² Following the conventional formal charges of the Na and S atoms, Na₃S can be expressed as [Na₃S]⁺·e⁻. To verify the contribution of interstitial electrons, an empty sphere was added into the channel voids with a radius of 1.50 Å. As shown in Fig. 4b, the Fermi level is dominantly contributed by the interstitial electrons, higher than the S and Na atoms. Thus, analogous to the electrides of Ca₂N,²¹ in which the ‘interstitial electrons’ serve as an electrical pathway, the infinite 1-D electron gas in the 1-D electride [Na₃S]⁺·e⁻ is assumed to contribute to the metallic character.

Metallic Na₅S₃. The electronic structure of Na₅S₃ is illustrated in Fig. 3. In the band structure (Fig. 3a), there is a dispersed band in the energy range from 4.91 eV to -0.11 eV (denoted as ‘band α ’) across the Fermi level, leading to metallic

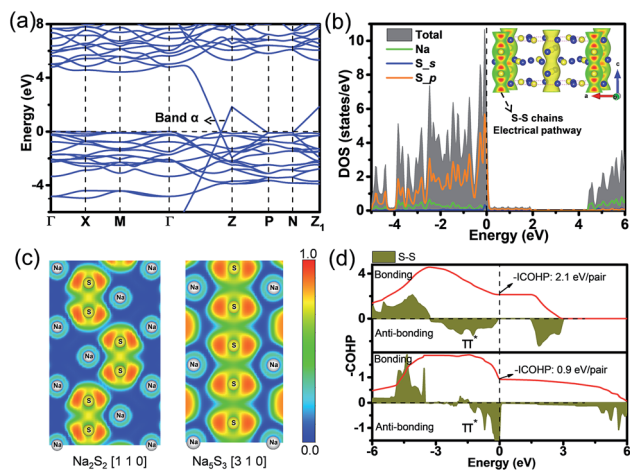


Fig. 3 Electronic properties for Na_5S_3 . (a) Calculated band structure. (b) Total and partial density of states (TDOS and PDOS). (c) Electron localization functions (ELFs) of Na_2S_2 ($P6_3/mmc$) in the $[110]$ plane and Na_5S_3 ($I4/mcm$) in the $[310]$ plane. (d) Calculated orbital Hamilton population curves ($-\text{COHP}$) of the S–S pairs in Na_2S_2 (top) and predicted Na_5S_3 (bottom). The inset in the density of states diagram is the partial charge density of 'band α ', while the inserted red curves in the $-\text{COHP}$ curves are the $-\text{COHP}$ integration ($-\text{ICOHP}$).

character. Partial density of states (PDOS) reveals that the Fermi level of Na_5S_3 is contributed dominantly by the S-3p orbitals (Fig. 3b), suggesting quite a different conductive mechanism from Na_3S . As shown in the partial charge density of 'band α ' (inset of Fig. 3b), all the electrons that are confined in 'band α ' are distributed in the sulfur chains. Thus, the S–S bonding in the sulfur chains is responsible for the metallic character of Na_5S_3 .

To unambiguously uncover the bonding character in sulfur chains, the orbital Hamilton population curves (COHP) and ELFs for Na_5S_3 are calculated and displayed in Fig. 3c and d, in comparison with semiconducting Na_2S_2 ($P6_3/mmc$). As shown in Fig. 3c, the high ELF value (about 0.75) can be observed in S_2 units in $P6_3/mmc$ - Na_2S_2 , explaining the strong S–S covalent bonding character; however the S–S chains in Na_5S_3 have a relatively lower value of ELF (0.5) between the nearest S atoms, which also suggests a metallic bonding character. The S–S bonding difference in Na_2S_2 (covalent) and Na_5S_3 (metallic) is also reflected by the COHP integration ($-\text{ICOHP}$) (Fig. 3d). The $-\text{ICOHP}$ value of S–S pairs in Na_2S_2 (2.3 eV per pair) is much greater than that of Na_5S_3 (0.9 eV per pair), revealing that the S–S bonding in Na_2S_2 is much stronger than that of Na_5S_3 . In the COHP curves, the antibonding in S–S pairs notably appears in the energy region from -3.3 eV to 0.0 eV in Na_2S_2 and -1.5 eV to 0.18 eV in Na_5S_3 , which corresponds to the S–S π_{p-p}^* bonding. Similar features are also observed in other chalcogenides, e.g., Ba_2SnSe_5 ,⁶³ and $\text{Co}_{1-x}\text{Fe}_x\text{S}_2$.⁶⁴ The metallic character of Na_5S_3 is thus dominated by the metallic S–S π_{p-p}^* bonding, where the metallic S–S infinite chains serve as an electrical pathway.

Since there are two non-equivalent S atoms in Na_5S_3 with a coordination of 10 (separated S_1) and 8 (S_2 in S–S chains) Na atoms, the Bader charge⁶⁵ is thus calculated for Na_5S_3 .

Intriguingly, the S atoms exhibit a mixed valence state with -1.60 and -0.87 for the S_1 and S_2 atoms, respectively. Due to the general underestimation of Bader charge, the valence state for S_1 and S_2 can be found with -2 and -1 , respectively. Such mixed valence states were first observed in alkali metal sulfides.

Semiconducting Na_2S_2 and Na_2S_3 . The electronic structure of predicted Na_2S_2 ($Pbam$) and Na_2S_3 ($Pnma$) is displayed in Fig. S4a–d.† The band structure of Na_2S_2 (Fig. S4a†) and Na_2S_3 (Fig. S4b†) exhibits semiconducting character with an indirect band gap of 0.96 eV and 1.14 eV within the PBE method. HSE06 functional enlarges the band gap to 2.02 eV and 2.28 eV as expected. As shown in the density of states plots (Fig. S4c and d†), the S–p orbitals show the dominant contribution to the density of states around the Fermi level, indicating that the S–S interactions are responsible for the semiconducting behaviors in Na_2S_2 and Na_2S_3 . The S–S bonding character in sulfur poly-anions can be verified by ELF analysis (inset of Fig. S4c and d†). The magnitude of the ELF values between the nearest sulfur atoms is 0.76 for S_2^{2-} (Na_2S_2) and 0.81 for S_3^{2-} (Na_2S_3), suggesting strong covalent bonding character in the S–S interaction.

Voltagages for Na–S batteries

To evaluate the electrochemistry performance of the experimental and predicted Na–S phases, we calculated the capacities and voltage for discharging reactions (Fig. 4). The calculated capacities are 334 , 418 , 836 and 1672 mA h g^{-1} for the

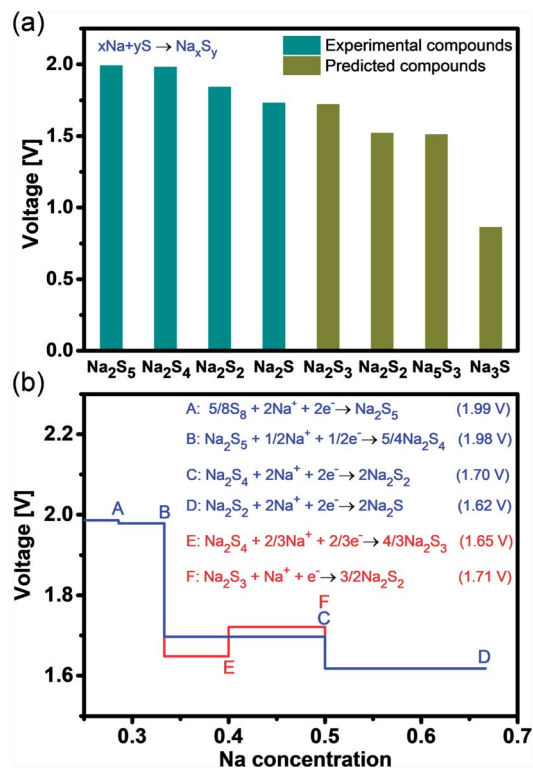


Fig. 4 (a) Voltages relative to Na for discharging overall-cell reactions of $x\text{Na} + y\text{S} \rightarrow \text{Na}_x\text{S}_y$. (b) Voltage profile of a Na–S battery as a function of Na concentrations.

experimental phases of Na_2S_5 , Na_2S_4 , Na_2S_2 , and Na_2S , respectively; and 557, 836, 1394 and 2508 mA h g^{-1} for the predicted phases of Na_2S_3 , Na_2S_2 , Na_5S_3 , and Na_3S , respectively. The voltages for the discharging overall-cell reactions: $x\text{Na} + y\text{S} \rightarrow \text{Na}_x\text{S}_y$ are illustrated in Fig. 4a, which shows the negative correlation with sodium concentrations. We also calculated the voltage profile between pairs of proximate phases relative to Na metal (Fig. 4b), using experimental phases (Na_2S_5 , Na_2S_4 , Na_2S_2 , and Na_2S) combined with our predicted Na_2S_3 . The voltages for reactions A and B generate Na_2S_5 and Na_2S_4 , yielding the values of 1.99 V and 1.98 V, respectively, which agree well with the experimental values of 2.20–1.65 V (reactions produce Na_2S_6 , Na_2S_5 and Na_2S_4).⁹ The voltages for reactions that produce Na_2S_2 (reactions C and F), Na_2S_3 (reaction E) and Na_2S (reaction D) range from 1.62 V to 1.71 V, consistent with experimental values (1.65 V, involving reactions that produce Na_2S_3 , Na_2S_2 , and Na_2S through Na_2S_4).⁹ Significantly, the voltage of the reactions from E $\left(\text{Na}_2\text{S}_4 + \frac{2}{3}\text{Na}^+ + \frac{2}{3}\text{e}^- \rightarrow \frac{4}{3}\text{Na}_2\text{S}_3\right)$ to F $\left(\text{Na}_2\text{S}_3 + \text{Na}^+ + \text{e}^- \rightarrow \frac{3}{2}\text{Na}_2\text{S}_2\right)$ containing Na_2S_3 increases from 1.65 V to 1.71 V. The increased voltages during the discharging process may be caused by multiple chemical reactions occurring in the electrochemical process.

Conclusions

In conclusion, we performed extensive structure searches to investigate the phase diversity and electronic properties of the Na–S system at ambient and high pressure. We successfully reproduced the phase transformations of Na_2S at 2.7 GPa and 12.2 GPa ($Fm\bar{3}m\text{-}Pnma\text{-}P6_3/mmc$). The experimental phases Na_2S_2 , Na_2S_4 , and Na_2S_5 became metastable at 7.0 GPa, 7.2 GPa, and 0.9 GPa, respectively. Among them, Na_2S_2 ($P6_3/mmc$) converted to a predicted highly packaged structure ($Pbam$) at 7.0 GPa. On the other hand, we identified three new stoichiometries, *i.e.*, Na_3S ($P6_3/mmc$), Na_5S_3 ($I4/mcm$), and Na_2S_3 ($Pnma$), which stabilized at 23.8 GPa, 3.2 GPa, and 0.9 GPa, respectively. In particular, under ambient conditions, Na_2S_3 possesses quite low formation enthalpy relative to Na_2S_2 and Na_2S_4 ($\text{Na}_2\text{S}_2 + \text{Na}_2\text{S}_4 \rightarrow 2\text{Na}_2\text{S}_3$; $\Delta H = 4.8$ meV per atom). Moreover, the crystal structure of Na_2S_3 with S_3^{2-} polyanions can be regarded as the transformation of previously synthesized $\text{Na}_2\text{S}_3 \cdot \text{NH}_3$ through ammonia removal. Thus, Na_2S_3 could be generated under non-equilibrium conditions (under high pressure or during an electrochemical process). In the simulated discharge reactions in the Na–S battery, the voltage through Na_2S_4 to generate Na_2S_3 is predicted to be 1.65 V, consistent with the experimental measurement. Detailed electronic structure analyses revealed that Na_3S is a potential 1-D electride with the chemical formula $[\text{Na}_3\text{S}]^+ \cdot \text{e}^-$. Na_3S and Na_5S_3 exhibit an intrinsic metallic behavior with two distinct conducting mechanisms: (1) the 1-D electron gas in the interstitial voids of $[\text{Na}_3\text{S}]^+ \cdot \text{e}^-$. (2) Exotic infinite sulfur chains with metallic S–S bonding in Na_5S_3 .

Conflicts of interest

There are no conflicts to declare.

Acknowledgements

This project was supported by the National Natural Science Foundation of China (NSFC) under Grant No. U1530402 and the Thousand Youth Talents Plan.

Notes and references

- 1 T. Oshima, M. Kajita and A. Okuno, *Int. J. Appl. Ceram. Technol.*, 2004, **1**, 269–276.
- 2 S.-W. Kim, D.-H. Seo, X. Ma, G. Ceder and K. Kang, *Adv. Energy Mater.*, 2012, **2**, 710–721.
- 3 V. Palomares, P. Serras, I. Villaluenga, K. B. Hueso, J. Carretero-González and T. Rojo, *Energy Environ. Sci.*, 2012, **5**, 5884–5901.
- 4 B. L. Ellis and L. F. Nazar, *Curr. Opin. Solid State Mater. Sci.*, 2012, **16**, 168–177.
- 5 K. B. Hueso, M. Armand and T. Rojo, *Energy Environ. Sci.*, 2013, **6**, 734–749.
- 6 J. T. Kummer and N. Weber, *SAE Int.*, 1968, **76**, 1003–1028.
- 7 B. R. Karas, *J. Electrochem. Soc.*, 1985, **132**, 1261–1266.
- 8 N. Tanibata, M. Deguchi, A. Hayashi and M. Tatsumisago, *Chem. Mater.*, 2017, **29**, 5232–5238.
- 9 A. Manthiram and X. Yu, *Small*, 2015, **11**, 2108–2114.
- 10 X. Yu and A. Manthiram, *J. Phys. Chem. Lett.*, 2014, **5**, 1943–1947.
- 11 J. Sangster and A. D. Pelton, *J. Phase Equilib.*, 1997, **18**, 89.
- 12 H. Momida, T. Yamashita and T. Oguchi, *J. Phys. Soc. Jpn.*, 2014, **83**, 124713.
- 13 T. Chivers and C. Lau, *Int. J. Hydrogen Energy*, 1985, **10**, 21–25.
- 14 F. Fehér and H. J. Berthold, *Z. Anorg. Allg. Chem.*, 1953, **273**, 144–160.
- 15 A. P. Brown and J. E. Battles, *Synth. React. Inorg. Met.-Org. Chem.*, 1984, **14**, 945–951.
- 16 P. Böttcher, *Z. Anorg. Allg. Chem.*, 1980, **467**, 149–157.
- 17 J. Zhao, Z. Lu, N. Liu, H.-W. Lee, M. T. McDowell and Y. Cui, *Nat. Commun.*, 2014, **5**, 5088.
- 18 Z. Zeng, Q. Zeng, N. Liu, A. R. Oganov, Q. Zeng, Y. Cui and W. L. Mao, *Adv. Energy Mater.*, 2015, **5**, 1500214.
- 19 S. Wang, J. Liu and Q. Sun, *J. Mater. Chem. A*, 2017, **5**, 16936–16943.
- 20 S. Wang, J. Liu, Y. Qie, S. Gong, Q. Sun and P. Jena, *J. Mater. Chem. A*, 2018, **6**, 18449–18457.
- 21 H. Tang, B. Wan, B. Gao, Y. Muraba, Q. Qin, B. Yan, P. Chen, Q. Hu, D. Zhang, L. Wu, M. Wang, H. Xiao, H. Gou, F. Gao, H. Mao and H. Hosono, *Adv. Sci.*, 2018, 1800666.
- 22 Y. Akahama, H. Kawamura, D. Häusermann, M. Hanfland and O. Shimomura, *Phys. Rev. Lett.*, 1995, **74**, 4690–4693.
- 23 H. Luo, S. Desgreniers, Y. K. Vohra and A. L. Ruoff, *Phys. Rev. Lett.*, 1991, **67**, 2998–3001.

- 24 O. Degtyareva, E. Gregoryanz, M. Somayazulu, H. Mao and R. J. Hemley, *Phys. Rev. B: Condens. Matter Mater. Phys.*, 2005, **71**, 214104.
- 25 Y. Akahama, M. Kobayashi and H. Kawamura, *Phys. Rev. B: Condens. Matter Mater. Phys.*, 1997, **56**, 5027–5031.
- 26 V. Y. Rokhorenko, B. I. Sokolovskii, V. A. Alekseev, A. S. Basin, S. V. Stankus and V. M. Sklyarchuk, *Phys. Status Solidi B*, 1982, **113**, 453–458.
- 27 N. F. Mott and E. A. Davis, *Electronic processes in Non-Crystalline Materials*, Oxford University Press, Oxford, 2012.
- 28 S. Urbonaitė, T. Poux and P. Novák, *Adv. Energy Mater.*, 2015, **5**(16), 1500118.
- 29 G. Yang, S. Shi, J. Yang and Y. Ma, *J. Mater. Chem. A*, 2015, **3**, 8865–8869.
- 30 C. Kokail, C. Heil and L. Boeri, *Phys. Rev. B*, 2016, **94**, 060502.
- 31 A. Vegas, A. Grzechnik, K. Syassen, I. Loa, M. Hanfland and M. Jansen, *Acta Crystallogr., Sect. B: Struct. Sci.*, 2001, **57**, 151–156.
- 32 A. R. Oganov and C. W. Glass, *J. Chem. Phys.*, 2006, **124**, 244704.
- 33 Y. Wang, J. Lv, L. Zhu and Y. Ma, *Comput. Phys. Commun.*, 2012, **183**, 2063–2070.
- 34 Y. Wang, J. Lv, L. Zhu and Y. Ma, *Phys. Rev. B: Condens. Matter Mater. Phys.*, 2010, **82**, 094116.
- 35 Y. Ma, M. Eremets, A. R. Oganov, Y. Xie, I. Trojan, S. Medvedev, A. O. Lyakhov, M. Valle and V. Prakapenka, *Nature*, 2009, **458**, 182.
- 36 J. P. Perdew, K. Burke and M. Ernzerhof, *Phys. Rev. Lett.*, 1996, **77**, 3865–3868.
- 37 G. Kresse and J. Furthmüller, *Comput. Mater. Sci.*, 1996, **6**, 15–50.
- 38 J. Klimeš, D. Bowler and A. Michaelides, *J. Phys.: Condens. Matter*, 2010, **22**, 022201.
- 39 J. Klimeš, D. R. Bowler and A. Michaelides, *Phys. Rev. B: Condens. Matter Mater. Phys.*, 2011, **83**, 772.
- 40 P. E. Blöchl, *Phys. Rev. B: Condens. Matter Mater. Phys.*, 1994, **50**, 17953–17979.
- 41 G. Kresse and D. Joubert, *Phys. Rev. B: Condens. Matter Mater. Phys.*, 1999, **59**, 1758–1775.
- 42 J. D. Pack and H. J. Monkhorst, *Phys. Rev. B: Solid State*, 1977, **16**, 1748–1749.
- 43 A. Togo and I. Tanaka, *Scr. Mater.*, 2015, **108**, 1–5.
- 44 S. Maintz, V. L. Deringer, A. L. Tchougréeff and R. Dronskowski, *J. Comput. Chem.*, 2016, **37**, 1030–1035.
- 45 R. Dronskowski and P. E. Blochl, *J. Phys. Chem.*, 1993, **97**, 8617–8624.
- 46 V. L. Deringer, A. L. Tchougréeff and R. Dronskowski, *J. Phys. Chem. A*, 2011, **115**, 5461–5466.
- 47 M. K. Aydinol, A. F. Kohan, G. Ceder, K. Cho and J. Joannopoulos, *Phys. Rev. B: Condens. Matter Mater. Phys.*, 1997, **56**, 1353–1365.
- 48 W. Zhang, A. R. Oganov, A. F. Goncharov, Q. Zhu, S. E. Boulfelfel, A. O. Lyakhov, E. Stavrou, M. Somayazulu, V. B. Prakapenka and Z. Konôpková, *Science*, 2013, **342**, 1502–1505.
- 49 K. Seifert-Lorenz and J. Hafner, *Phys. Rev. B: Condens. Matter Mater. Phys.*, 2002, **66**, 094105.
- 50 P. Coppens, Y. W. Yang, R. H. Blessing, W. F. Copper and F. K. Larsen, *J. Am. Chem. Soc.*, 1977, **99**, 760–766.
- 51 S. Yamaoka, J. T. Lemley, J. M. Jenks and H. Steinfink, *Inorg. Chem.*, 1975, **14**, 129–131.
- 52 P. Böttcher, *Z. Anorg. Allg. Chem.*, 1977, **432**, 167–172.
- 53 Z. Wu, E. Zhao, H. Xiang, X. Hao, X. Liu and J. Meng, *Phys. Rev. B: Condens. Matter Mater. Phys.*, 2007, **76**, 054115.
- 54 A. V. Krukau, O. A. Vydrov, A. F. Izmaylov and G. E. Scuseria, *J. Chem. Phys.*, 2006, **125**, 3865.
- 55 A. Savin, R. Nesper, S. Wengert and T. F. Fassler, *Angew. Chem., Int. Ed. Engl.*, 1997, **36**, 1808–1832.
- 56 Y. Zhang, Z. Xiao, T. Kamiya and H. Hosono, *J. Phys. Chem. Lett.*, 2015, **6**, 4966–4971.
- 57 S. Matsuishi, Y. Toda, M. Miyakawa, K. Hayashi, T. Kamiya, M. Hirano, I. Tanaka and H. Hosono, *Science*, 2003, **301**, 626–629.
- 58 B. Wan, Y. Lu, Z. Xiao, Y. Muraba, J. Kim, D. Huang, L. Wu, H. Gou, J. Zhang, F. Gao, H. Mao and H. Hosono, *npj Comput. Mater.*, 2018, **4**, 77.
- 59 M.-S. Miao and R. Hoffmann, *Acc. Chem. Res.*, 2014, **47**, 1311–1317.
- 60 M. Miao and R. Hoffmann, *J. Am. Chem. Soc.*, 2015, **137**, 3631–3637.
- 61 Y. Lu, J. Li, T. Tada, Y. Toda, S. Ueda, T. Yokoyama, M. Kitano and H. Hosono, *J. Am. Chem. Soc.*, 2016, **138**, 3970–3973.
- 62 L. A. Burton, F. Ricci, W. Chen, G.-M. Rignanese and G. Hautier, *Chem. Mater.*, 2018, **30**, 7521–7526.
- 63 M. Zelinska, A. Assoud, C. Graf and H. Kleinke, *Inorg. Chem.*, 2010, **49**, 1090–1093.
- 64 K. Ramesha, R. Seshadri, C. Ederer, T. He and M. A. Subramanian, *Phys. Rev. B: Condens. Matter Mater. Phys.*, 2004, **70**, 214409.
- 65 E. Sanville, S. D. Kenny, R. Smith and G. Henkelman, *J. Comput. Chem.*, 2007, **28**, 899–908.